

# High Capacity Mg Batteries Based on Surface-Controlled Electrochemical Reactions

Lu Wang,<sup>a</sup> Per Erik Vullum,<sup>b,c</sup> Karina Asheim,<sup>a</sup> Xuehang Wang,<sup>d</sup> Ann Mari Svensson,<sup>a</sup> and Fride Vullum-Bruer<sup>\*a</sup>

<sup>a</sup>Department of Materials Science and Engineering, Norwegian University of Science and Technology, NO-7491 Trondheim, Norway

<sup>b</sup>SINTEF Materials and Chemistry, 7491 Trondheim, Norway

<sup>c</sup>Department of Physics, Norwegian University of Science and Technology, 7491 Trondheim, Norway

<sup>d</sup>Department of Chemical Engineering, Norwegian University of Science and Technology, 7491 Trondheim, Norway.

## ABSTRACT

Mg batteries are one of several new battery technologies expected to partially substitute lithium-based batteries in the future due to the lower cost and higher safety. However, the development of Mg batteries has been greatly hindered by the sluggish Mg migration kinetics in the solid state. Here, we exploit a high performance cathode for Mg battery based on a tailored nanocomposite, synthesized by *in-situ* growth of nanocrystalline Mn<sub>3</sub>O<sub>4</sub> on graphene substrates, which provides high reversible capacities (~220 mAh g<sup>-1</sup> at 15.4 mA g<sup>-1</sup> and ~80 mAh g<sup>-1</sup> at 1.54 A g<sup>-1</sup>), good rate performance (high reversibility at various current rates), and excellent cycling stability (no capacity decay after 700 hundred cycles). The magnesiation mechanism in our cell system has been identified as a combination of capacitive processes and diffusion-controlled reactions involving electrolyte solvents. Characterization is performed by *ex-situ* transmission electron microscopy (TEM)/scanning TEM (STEM), energy dispersive spectroscopy (EDS), electron energy loss spectroscopy (EELS) and X-ray photoelectron spectroscopy (XPS) in addition to quantitative kinetics analysis. Exploiting the high-performance capacitive-type electrodes, where the specific capacity is limited by the kinetics of surface processes and not by bulk Mg ion diffusion governing the properties of conventional intercalation-type electrodes, could reveal a new approach to developing commercially viable Mg batteries.

**KEYWORDS:** Mg batteries; high performance cathode; Mn<sub>3</sub>O<sub>4</sub>; capacitive processes; diffusion-controlled reactions.

## 1. Introduction

Manganese oxides, as the typical transition metal oxides, have been known as high voltage cathodes for Mg batteries due to operating voltages in excess of 3.0 V *vs.* Mg [1]. However, the stable potential window of most Mg electrolytes does not meet the requirements of Mg intercalation into manganese oxides [2-4]. Especially, the typical Mg organohaloaluminate electrolyte, all phenyl complex (APC) electrolyte, limits the cell potential to 2.2 V *vs.* Mg owing to the existence of stainless steel components in the coin cell, which can potentially be corroded by the chloride species in the electrolyte [5-7]. Even for the newly developed inorganic electrolytes (Mg-Al chloride complex electrolyte, which is referred to as MACC electrolyte) [8], and the non-halide electrolytes (Mg(PF<sub>6</sub>)<sub>2</sub>-based electrolytes [9], Mg(TFSI)<sub>2</sub>-based electrolytes [10], Mg(BH<sub>4</sub>)<sub>2</sub>-based electrolytes [11]), the capacity and cycling stability are poor due to extremely sluggish bulk diffusion kinetics of the Mg<sup>2+</sup> cations in the metal oxide hosts. Only a few classes of compounds developed thus far meet the requirements of reversible Mg intercalation/de-intercalation, such as the Chevrel-phase compounds (based on Mo<sub>6</sub>S<sub>8</sub>) [12,13], MoO<sub>3</sub> [14-16], MoS<sub>2</sub> [17,18], V<sub>2</sub>O<sub>5</sub> [16,19], and Ti<sub>2</sub>S<sub>4</sub> [20]. The narrow choice of electrode materials hinders the development of the Mg battery to be equally successful as the Li battery or Na battery technology.

In contrast to the sluggish Mg intercalation kinetics, the capacitive processes, which are normally the mechanism observed in supercapacitors, feature fast kinetics and high reversibility over time since there are no phase changes. This creates a system with charge and discharge performances, which are more characteristic of a capacitor than a battery (high rate capability and long cycling stability) [21,22]. In light of this point, utilization and development of a capacitive cell configuration is of interest to high power density applications [21]. So far, the enhanced capacities have been achieved in several Li battery and Na battery electrode materials. Bruce *et al.* demonstrated that both the capacitive contribution and the total stored charge significantly increased when decreasing the particle size of TiO<sub>2</sub> electrode in a Li battery configuration [21]. Similar capacitive effects also arise in Na battery systems where graphene foam supported tin sulfide nanosheets were used as anode, according to the study reported by Shen *et al.* [22].

Inspired by the capacitive characteristics in Li and Na batteries, several electrode materials for Mg batteries with capacitor-like behavior have been reported [2,24,25]. One of these, the Mn<sub>3</sub>O<sub>4</sub> nanoparticles, is reported in our previous work to exhibit very high cycling stability [3]. An almost straight line is observed for the galvanostatic charge/discharge profiles of the Mn<sub>3</sub>O<sub>4</sub> cathode in APC-tetrahydrofuran (THF) electrolyte. This is a typical feature for the capacitive-controlled charge storage mechanism, which gives rise to the excellent reversibility and long-term cycling stability. Interestingly, several plateau-looking features can also be observed in the charge/discharge profiles of the Mn<sub>3</sub>O<sub>4</sub> cathode, which correspond to the redox peaks in the CV curves. This is an indication that redox reactions do occur during cycling. These redox reactions are most likely related to the THF solvent and occur at the electrode/electrolyte interface. At this interface, the Mg monomer-[MgCl·5THF]<sup>+</sup>, which is decomposed from Mg dimer-[Mg<sub>2</sub>(μ-Cl)<sub>3</sub>·6THF]<sup>+</sup> in the bulk electrolyte, is the active Mg species involved in the charge transfer [26]. However, the Mg complex have a low degree of dissociation at the

interface due to the high charge density of Mg cations. Thus, the partly desolvated Mg monomers may be formed at this interface, which hinders Mg intercalation in most host materials. Gewirth *et al.* indicated that in the presence of the Lewis acidity of  $\text{RMg}^+$ , the THF molecules coordinated to the Mg-complex, are more easily oxidized to GBL at the interface [27,28]. Meanwhile, there are probably several intermediate products during the oxidation of THF to GBL co-formed at the interface (e.g. 2-hydroxytetrahydrofuran [29], 2,2-dihydroxytetrahydrofuran [30] and THF peroxide [31,32]). All of the above THF-related interfacial reactions make the chemical system at the interface complicated and the complete understanding of the THF-related interfacial reactions is still lacking. Aurbach *et al.* also proved by NMR and Raman spectroscopy that the chemical system in Mg organohaloaluminates (e.g. APC) is far more complex than the electrolytes of Li batteries [33]. Nevertheless, these little-known interfacial reactions in the  $\text{Mn}_3\text{O}_4$ -APC cell are at least confirmed to be highly reversible according to the high cycling stability of the  $\text{Mn}_3\text{O}_4$  cathode [3]. Analogously, Song *et al.* revealed that the THF molecules and other species in the APC-THF electrolyte could be involved in the interfacial redox reactions during cycling, according to the surface analysis by XPS of the cycled electrodes, thus providing a substantial capacity [34]. Here, the capacitive charge storage mechanisms in the  $\text{Mn}_3\text{O}_4$ -APC cell has been studied further, with the combination of *ex-situ* characterizations (TEM/STEM, EDS, EELS and XPS) and kinetics analysis (which is based on the CV curves). The charge storage mechanism is identified as a combination of the capacitive process (~80%) and the interfacial redox reactions involving the electrolyte solvents (~20%). In order to enhance the rate capability of the  $\text{Mn}_3\text{O}_4$  electrode, graphene nanosheets with varying amounts of oxygen functional groups were used as the substrate for supporting the  $\text{Mn}_3\text{O}_4$  nanoparticles. This serves to increase the number of active sites for charge storage, and is a method that has also been widely used to achieve improved capacities in supercapacitors [35-39]. The  $\text{Mn}_3\text{O}_4$ /partly reduced graphene oxide (RGO) nanocomposite delivers the high reversible capacities of ~220 mAh  $\text{g}^{-1}$  at 15.4 mA  $\text{g}^{-1}$  and ~80 mAh  $\text{g}^{-1}$  at 1.54 A  $\text{g}^{-1}$ . In addition, no capacity decay was observed after 700 cycles. The cell system proposed here seems to be a promising strategy for solving the issues encountered with the intercalation-based electrodes in Mg batteries.

## 2. Experimental section

### 2.1 Synthesis of $\text{Mn}_3\text{O}_4$ Nanoparticles

$\text{Mn}_3\text{O}_4$  nanoparticles were prepared by using the same procedure as in our previous work [3]. In short,  $\text{MnCl}_2 \cdot 4\text{H}_2\text{O}$  (Aldrich, 99%) was first dissolved in ethanol amine (ETA, Aldrich, 99%) while exposed to ultrasonic waves (Branson digital sonifier, Danbury, USA). The mixture was then stirred overnight after the distilled water was introduced. Through the processing of centrifugation, washing and drying, dark brown  $\text{Mn}_3\text{O}_4$  powders with uniform particle size of ~7-10 nm were obtained. Commercially available  $\text{Mn}_3\text{O}_4$  with larger particle sizes of ~100 nm (C- $\text{Mn}_3\text{O}_4$ , Erachem Comilog) was used without further treatment to study the magnesiation mechanism.

## 2.2 Synthesis of Graphene Oxide (GO) Suspension

First, graphite oxide (GiO) was synthesized by using a modified Hummers' method [40]. Then, the obtained GiO powders were dispersed in distilled water. After the ultrasonic treatment of aqueous GiO, exfoliated was performed to obtain GO. Finally, the GO suspension was obtained when the un-exfoliated GiO was removed by centrifugation (10 min, 3000 rpm).

## 2.3 Synthesis of *MGO* Nanocomposite

The synthesis of *MGO* ( $\text{Mn}_3\text{O}_4$ /graphene oxide) and *MRGO* nanocomposites have been reported in previous work [41] and is illustrated in Scheme 1. The  $\text{MnCl}_2$ /ETA solution and GO suspension were thoroughly mixed by stirring overnight. Then, the *MGO* nanocomposite was obtained through similar procedures to that used in the preparation of  $\text{Mn}_3\text{O}_4$  (centrifugation, washing and drying).

## 2.4 Synthesis of *MRGO* Nanocomposites

The GO suspension (0.2 g GO) and varying amounts (depending on the desired degree of reduction) of hydrazine solution (5 wt% in water) were mixed in a 500 mL three-necked flask under stirring at  $\sim 85^\circ\text{C}$  for 1h. The  $\text{MnCl}_2$ /ETA (15 mmol  $\text{MnCl}_2$ ) solution was then added to the resulting RGO (partly reduced graphene oxide) suspension. After stirring overnight at  $\sim 85^\circ\text{C}$ , the *MRGO* nanocomposites were obtained through similar procedures to that used in the  $\text{Mn}_3\text{O}_4$  preparation (centrifugation, washing and drying). Here, several *MRGO* nanocomposites with different amounts of oxygen-groups were prepared by changing the mass ratio of GO/hydrazine. The ratio equals to 1:1 for *MRGO-1*, 1:2 for *MRGO-2*, 1:4 for *MRGO-4* and 1:8 for *MRGO-8*.

## 2.5 Preparation of APC-THF Electrolytes

The APC-tetrahydrofuran (THF) (THF, Aldrich, anhydrous) electrolyte was synthesized according to the procedure reported by Aurbach's group [42]. Briefly,  $\text{AlCl}_3$  ( $\text{AlCl}_3$ , Aldrich, 99.999%)-THF solution was mixed with  $\text{PhMgCl}$ -THF solution ( $\text{PhMgCl}$  in THF, Aldrich, 99%) with a molar ratio of 1:2. The obtained mixture was stirred at least 24 hours before it was used. The whole preparation process was performed in an Ar-filled glove box ( $<0.1$  ppm of water and oxygen) due to the moisture sensitivity of the electrolyte. In this study, the concentration of the APC electrolyte was  $0.4 \text{ mol L}^{-1}$ .

## 2.6 Material Characterizations

The elemental analyses of the synthesized samples were performed by a VarioEL III elemental analyzer (Elementar, Germany). XRD measurements were done on a Bruker AXS D8 FOCUS diffractometer with  $\text{Cu K}\alpha$  radiation and a Lynxeye detector. Brunauer-Emmett-Teller (BET) surface areas were measured on a Micrometrics Tristar 3000 instrument through  $\text{N}_2$  adsorption isotherms at liquid nitrogen temperature. In order to eliminate the adsorbed water, the samples were degassed at  $120^\circ\text{C}$  under vacuum overnight before the measurements. ATR-FTIR measurements were performed on a Bruker Optiks IFS66V S-1 with the scanning resolution of  $2 \text{ cm}^{-1}$  and the scanning number of 68. As a mercury-cadmium-telluride (MCT)

detector and the internal reflectance element, a microscope (HYPERION 3000) was fitted with an ATR objective. The Raman spectroscopy measurements were carried out on a micro-Raman system (Renishaw, DM2500-In Via). The excitation energy was 2.41 eV (514 nm). The electrical conductivity ( $\sigma_E$ ) was measured by using a Kelvin bridge and calculated by the following equation [43]:

$$\sigma_E = [R_{\text{measured}} \frac{S}{H}]^{-1}$$

where  $R_{\text{measured}}$  is the measured electrical resistance (0.01  $\mu\Omega$  - 1000  $\Omega$ ),  $S$  is the cross section of the powder column and  $H$  is its height.

XPS analysis was performed by using a Kratos Axis Ultra DLD spectrometer with a monochromatic  $Al_{K\alpha}$  radiation ( $h\nu = 1486.6$  eV). TEM was performed with a double Cs corrected coldFEG JEOL ARM200CF, operated at 200 kV and equipped with a large solid angle (0.98 srad) Centurio EDS detector and a Quantum ER GIF for EELS.

## 2.7 Electrochemical Measurements

The electrode slurry was made by ball milling a mixture consisting of 80 wt% of the as-synthesized sample, 10 wt% of Super-P carbon black and 10 wt% of polyvinylidene difluoride (PVDF, Kynar, reagent grade) in the presence of N-methyl pyrrolidinone (NMP, Aldrich, >99%). Then, the electrode film was formed by drop coating the slurry onto flexible graphite foil (Gif, Goodfellow, 99.8%), followed by drying at 120 °C under vacuum for 10 hours. The dried film was punched into discs with the diameter of 16 mm. The mass loading of the electrode is about 0.6 mg. The battery performance of the synthesized materials was examined using CR2016 coin cells with 0.4 mol L<sup>-1</sup> APC-THF electrolyte, glass microfiber separator (Whatman), and a 0.2 mm thick Mg ribbon counter electrode, which was polished on both sides with SiC paper, then washed clean with THF and dried overnight under vacuum. The cells were assembled in an Ar-filled glove box. Galvanostatic charge/discharge measurement was performed on a Maccor 4200 (Maccor Inc., USA) battery testing system at ambient temperature. The current densities varied from 15.4 mA g<sup>-1</sup> to 1.54 A g<sup>-1</sup>. All the specific capacities obtained in this work are related to the mass of the active material (*MGO* or *MRGO*). The specific capacities related to the mass of the electrodes (*MGO/MRGO* + Super-P + PVDF) are also shown in Table S1 in Supporting Information, together with the volumetric capacities. CV was measured by using a 3-electrode cell (EL-CELL), where the Mg ribbon acts as both reference- and counter electrode, on a Gamry Reference 600 instrument (Pennsylvania, USA).

A symmetrical cell using 1M MgCl<sub>2</sub> aqueous electrolyte was fabricated. Two electrodes with the same mass loading were used as the electrodes. The synthesized materials are all used as the active electrodes. The charge/discharge analysis is performed using both constant current density of 1-6 A g<sup>-1</sup> and constant scan rate of 50-500 mV s<sup>-1</sup> within the voltage range of 0-1 V.

### 3. Results and discussion

#### 3.1 Characterizations of the *MGO* and *MRGO* Nanocomposites

In this work, five different composites (*MGO* and *MRGO-1* to *MRGO-8*) were obtained with increased degree of reduction of the functional groups on the graphene substrate. In Fig. S1, XRD analysis showed that the  $\text{Mn}_3\text{O}_4$  nanoparticles grown on the surface of the GO nanosheets (GOs) or RGO nanosheets (RGOs) exhibited the same crystal structure as the  $\text{Mn}_3\text{O}_4$  synthesized in solution. The ATR-FTIR spectrum obtained from *MGO* demonstrated the presence of O-H ( $3400\text{ cm}^{-1}$ , carboxylic), C-O ( $1028\text{ cm}^{-1}$ , alkoxy) and C=C ( $1580\text{ cm}^{-1}$ , non-oxidized graphitic domains), as shown in Fig. S2 [44-47]. The characteristic peaks from the O-H and C-O bonds become much weaker in the spectra of *MRGO-1*, *MRGO-2* and *MRGO-4*, and almost disappeared in the spectrum of *MRGO-8*. The dramatic decrease of functional-groups from *MGO* to *MRGO-8* can be further verified according to their elemental analyses and electronic conductivities (see Table S2), which shows a continuous increase in the C/H and C/N ratios and conductivities due to the removal of O,H,N-containing groups by reduction [41]. The rapid increase in the C/H and C/N ratios of *MRGO-8* may be ascribed to the large amount of reducing agent (hydrazine solution) introduced during sample preparation, compared to *MRGO-4*.

As reported in previous work, the growth behaviour of  $\text{Mn}_3\text{O}_4$  nanoparticles is closely related to the functional groups of GOs and RGOs, which serve as the anchor sites for the *in-situ* formation of  $\text{Mn}_3\text{O}_4$  nanostructures [41]. The functional groups enable the anchored nuclei of  $\text{Mn}_3\text{O}_4$  to grow separately, resulting in the well dispersed  $\text{Mn}_3\text{O}_4$  nanoparticles on GO. On the other hand, during the preparation of *MRGO* nanocomposites, the relatively bigger  $\text{Mn}_3\text{O}_4$  agglomerates are wrapped inside the RGO due to the massive reduction of functional groups [41,48]. The changes in morphology from *MGO* to *MRGO-8* can be visually observed from the TEM images. Fig. 1a and 1b show homogeneous and dense  $\text{Mn}_3\text{O}_4$  nanoparticles well dispersed on the surface of GO. The diffraction rings indexed in the selected area electron diffraction (SAED) patterns of *MGO* shown in Fig. S3b all match the corresponding  $\text{Mn}_3\text{O}_4$  reflections observed in the XRD patterns. With moderate reduction, the  $\text{Mn}_3\text{O}_4$  nanoparticles are still well dispersed on the surface of the now more wrinkled RGO, as shown in Fig. 1c and 1d. However, Fig. 1e and 1f, which show the TEM images of the *MRGO-8* nanocomposite with the largest degree of reduction, clearly show different morphological features. The relatively large  $\text{Mn}_3\text{O}_4$  agglomerates seem to be wrapped in the curved RGO when most of the functional groups are removed, leading to weak  $\text{Mn}_3\text{O}_4$  diffraction rings compared to those of the uncovered  $\text{Mn}_3\text{O}_4$  crystals in *MRGO-4* (see Fig. S3c), and the strong six-fold symmetrical diffraction rings that feature the graphitic substrate (Fig. S3d). Such morphology disparities between *MGO* and *MRGO* nanocomposites also give rise to different BET surface areas. In Table S2, *MGO* displays a relatively higher surface area of  $\sim 160\text{ m}^2\text{ g}^{-1}$ , compared to  $\sim 120\text{ m}^2\text{ g}^{-1}$  for the *MRGO* nanocomposites. Incidentally, there is no significant relationship between the morphology features and the surface area, since the *MRGO* nanocomposites with different reduction degrees show similar surface areas. There is however, a significant relationship between the morphology features and the cell performance when these synthesized nanocomposites were

used as cathode materials in a Mg battery, which will be discussed further in the following sections.

### 3.2 Charge Storage Performance of the *MGO* and *MRGO* Nanocomposites

As shown in Fig. 2a and Fig. S4, all of the synthesized samples exhibit similar features in the charge/discharge profiles and CV curves, indicating that the charge storage mechanisms in *MGO* and *MRGO* nanocomposites are the same as in the  $\text{Mn}_3\text{O}_4$  nanoparticles. During the magnesianation process illustrated in Scheme 2, the Mg monomers, which served as the charge transfer active species at the electrode/electrolyte interface [26,49], adsorb on the electrode surface to provide the non-faradaic capacitive contribution. The coordinated THF molecules take part in the interfacial redox reactions in the presence of  $\text{MgCl}^+$  (which acts as a Lewis acid) to provide the faradaic capacity. The surface properties and morphology features of the synthesized materials determine the active sites for charge storage, which are crucial for the electrochemical performance of the synthesized materials as cathode in a Mg battery. Hence, on the one hand, stable cycling performances were observed in all the composites due to the fast kinetics of the capacitive process (see Fig. 2b). On the other hand, the values of the specific capacities vary significantly among the synthesized composites as shown in Fig. 2. In contrast to  $\text{Mn}_3\text{O}_4$ , the capacities keep increasing from *MRGO-1* to *MRGO-4* with the increase in conductivity. However, there is a quick drop in capacity from *MRGO-4* to *MRGO-8* (which exhibits the highest conductivity). This is probably related to the severely agglomerated  $\text{Mn}_3\text{O}_4$  particles in *MRGO-8*, which would reduce the active surface area available for electrochemical reactions, as illustrated in Scheme 2. Consequently, the *MRGO-4* nanocomposite with good particle dispersity (which ensures high utilization of active material) and enhanced conductivity (which benefits the charge diffusion along the RGOs substrate) shows the best performance as cathode in a Mg battery. This composite performs a reversible capacity of  $\sim 220 \text{ mAh g}^{-1}$  at  $15.4 \text{ mA g}^{-1}$  compared to  $\sim 100 \text{ mAh g}^{-1}$  for  $\text{Mn}_3\text{O}_4$  nanoparticles.<sup>6</sup> *MRGO-4* also exhibits high rate capability ( $\sim 80 \text{ mAh g}^{-1}$  at  $1.54 \text{ A g}^{-1}$  and  $\sim 100\%$  efficiency at different rates) and stable long term cycling performance (see Fig. 3a and 3b). Interestingly, with the highest surface area but lowest conductivity of all the composites, the *MGO* composite exhibits similar capacities and cycling stability to *MRGO-4*, as observed in Fig. S5. Previous work has shown *MGO* [41] as well as other GO-based composites to be promising electrodes for supercapacitors [50-54]. Although the charge transfer is hindered by the lower conductivity caused by the presence of the functional groups, the well-dispersed  $\text{Mn}_3\text{O}_4$  nanoparticles on the surface of the GO substrate are beneficial for the charge storage during cycling (see Scheme 2), resulting in the substantial capacitance. It may also be that the functional groups contribute to the charge storage through additional faradaic reactions [55], which also make GO promising electrodes for supercapacitors. As shown in Fig. S6, the GO cathode provides a reversible capacity of  $\sim 85 \text{ mAh g}^{-1}$  at  $15.4 \text{ mA g}^{-1}$ , indicating that the functional groups of GO in the capacitive-controlled Mg battery system can indeed improve capacity. In addition, due to the synergy effect between the  $\text{Mn}_3\text{O}_4$  nanoparticles and GO nanosheets, the *MGO* composite exhibits a higher capacity ( $\sim 220 \text{ mAh g}^{-1}$ ) than the sum of the capacities of the  $\text{Mn}_3\text{O}_4$  nanoparticles ( $\sim 100 \text{ mAh g}^{-1}$ ) and the GO nanosheets ( $\sim 85 \text{ mAh g}^{-1}$ ) measured separately. Similar charge storage tendencies were also observed when *MGO* and *MRGO* composites were used as electrodes in a symmetrical

cell configuration, where aqueous  $\text{MgCl}_2$  was used as electrolyte. Based on the rectangular features of the CV curves for the symmetrical cells shown in Fig. S7a and S7b, there are no redox reactions occurring during charge or discharge, only capacitive contributions are observed. The well dispersed  $\text{Mn}_3\text{O}_4$  nanoparticles and the abundant functional groups endow the MGO composite with equally high specific capacitance as that obtained for the *MRGO-4* composite, as shown in Fig. S7c. The *MRGO-8* composite on the other hand, shows much lower capacitance due to lower surface area caused by particle agglomeration and folding of the RGO sheets. The results obtained from the symmetrical cells bring us further proof of the large capacitive contribution to the overall capacity of the Mg batteries made with the  $\text{Mn}_3\text{O}_4$  composite cathodes. In addition, it is quite evident that there is a close relation between the capacitive contribution and the morphology features of the synthesized materials.

### 3.3 *Ex-situ* Characterizations of the $\text{Mn}_3\text{O}_4$ Cathode in Mg Battery Configuration

To further understand the charge storage mechanisms in the synthesized materials without the interference from the graphene substrate and the functional groups, *ex-situ* characterizations with TEM/STEM, EDS and EELS of the magnesiated and demagnesiated  $\text{Mn}_3\text{O}_4$  cathodes in APC-THF electrolyte were performed. As shown in Fig. 4a and 4b, the overlaid Mn-Mg map after the initial full discharge of the  $\text{Mn}_3\text{O}_4$  cathode in APC-THF electrolyte show that the Mg cations (corresponding to the red dots in Fig. 4b) are concentrated on the surface of the  $\text{Mn}_3\text{O}_4$  nanoparticles and can hardly be observed in the bulk. Note that the Mg signal should still be detected everywhere on the particle (see Fig. S8c) even if the Mg is only located on the surface of  $\text{Mn}_3\text{O}_4$  nanoparticles. TEM is a two-dimensional projection, where the obtained signal contains contributions from the top to the bottom surfaces of the  $\text{Mn}_3\text{O}_4$  nanoparticles. The relative Mg dispersion can be more clearly seen in the EDS map of the large sized C- $\text{Mn}_3\text{O}_4$  particles (which showed a low capacity of  $\sim 30 \text{ mAh g}^{-1}$  at  $15.4 \text{ mA g}^{-1}$  due to severe agglomeration [3]) in Fig. 5. And the Mg content in the bulk is negligible compared to that on the surface according to the EDS spectra of C- $\text{Mn}_3\text{O}_4$ . In addition, in Fig. 4e, the nearly overlapping Mn  $L_{2,3}$  edge spectra of the pristine and magnesiated  $\text{Mn}_3\text{O}_4$  cathodes corresponding to the bulk of the  $\text{Mn}_3\text{O}_4$  nanoparticles indicates no valence change of the Mn cations before and after magnesiation. This demonstrates that no intercalation of Mg cations occurred in the bulk of the  $\text{Mn}_3\text{O}_4$  particles, in accordance with the result obtained by *ex-situ* XRD characterizations from our previous work [3], where show that there is no new peak formation or peak shift during cycling of  $\text{Mn}_3\text{O}_4$  electrodes in APC-THF electrolyte. Interestingly, a small amount of Mg cations still resided on the surface after the following charge, as shown in Fig. 4d and Fig. S8f. This is probably caused by irreversible reactions during the initial discharge, trapping a certain amount of Mg in the surface layers, and could be a reasonable explanation for the capacity loss between the initial discharge and the following charge in  $\text{Mn}_3\text{O}_4$ -APC cell. The relative elemental contents (e.g. O, Mg and Mn) of the magnesiated and de-magnesiated  $\text{Mn}_3\text{O}_4$  cathodes are shown in Fig. 4f and 4g. It is known that EDS is only a semi-quantitative technique and the collected data has large systematic errors. But the relative change in the ratio, e.g. Mg/Mn ratio, is reliable since the systematic errors cancel out when comparing these two ratios. In this work, the Mg/Mn ratio of the magnesiated  $\text{Mn}_3\text{O}_4$  cathode is higher than that of the de-magnesiated  $\text{Mn}_3\text{O}_4$  cathode and the difference between these two ratios could be approximated to provide an equivalent of  $\sim 150 \text{ mAh g}^{-1}$

reversible capacity. This roughly calculated value is based on the hypothesis that the synthesized  $\text{Mn}_3\text{O}_4$  particles possess spherical morphology with a diameter of 10 nm and uniform density of  $4.86 \text{ g cm}^{-3}$ . And the value is close to the reversible capacity ( $\sim 100 \text{ mAh g}^{-1}$ ) found through galvanostatic charge/discharge measurements.

Furthermore, Fig. S9 shows the HAADF STEM image and elemental maps of one single magnesiated  $\text{Mn}_3\text{O}_4$  nanoparticle in APC-THF electrolyte, in combination with the comparison of Mn  $L_{2,3}$  electron energy loss edges between the surface and the bulk of the magnesiated  $\text{Mn}_3\text{O}_4$  cathodes. No chemical shift or change in the  $L_3/L_2$  ratio is observed between the bulk and the surface spectra, which represents no valence change of Mn at the surface of the  $\text{Mn}_3\text{O}_4$  nanoparticle [56]. The same conclusion can also be obtained by the *ex-situ* XPS characterizations of the  $\text{Mn}_3\text{O}_4$  cathodes at different cell states in APC-THF electrolyte shown in Fig. 6, which shows no shift of Mn 2p peaks during cycling. Incidentally, the slight difference in the O-K edge spectra observed in Fig. S9f may be caused by the interference from other O-containing complexes. In addition, no amorphous layer was observed on the surface of the  $\text{Mn}_3\text{O}_4$  nanoparticle by *ex-situ* TEM characterizations, as shown in Fig. 7. These results definitely exclude the possibility of intercalation or conversion reactions taking place on the surface of the  $\text{Mn}_3\text{O}_4$  nanoparticles in APC-THF electrolyte. Both the surface and the bulk of the  $\text{Mn}_3\text{O}_4$  nanoparticles remain crystalline after magnesiation. This phenomena where no phase changes occur during cycling, associated with the nearly linear charge/discharge profiles previously observed [3], signify that the capacitive processes dominate the charge storage mechanism and thus provide the high stability of the system during long-term cycling.

### 3.4 Kinetics and Quantitative Analysis of the $\text{Mn}_3\text{O}_4$ Cathode in Mg Battery Configuration

As Mg intercalation can be ruled out from the  $\text{Mn}_3\text{O}_4$  cathode, we mainly consider two charge storage mechanisms: the faradaic contribution from THF-related interfacial reactions and the contribution from the capacitive processes [57]. To shed light on the charge storage mechanism, the method of CV scan rate ( $v$ ) dependence proposed by Lindquist *et al.* was applied according to the power law:  $i = av^b$  [58], in which ( $i$ ) is the response current, and both  $a$  and  $b$  are adjustable parameters. The  $b$ -values can be determined from the linear plot of  $\log i$  vs.  $\log v$  with two well-defined critical values,  $b = 0.5$  and  $b = 1$ . A  $b$ -value of 0.5 is expected for diffusion-controlled reactions and processes, while a  $b$ -value of 1 indicate non-diffusion controlled processes [21,59]. For example, as shown in Fig. 8b and 8c, at the anodic peak of 0.68 V and the cathodic peak of 0.48 V, the  $b$ -values are 0.67 and 0.64, respectively. This indicates that the interfacial redox reactions are limited by the diffusion of the THF molecules. As Conway *et al.* elaborated in their studies, the redox reactions can be diffusion controlled if the redox reactants are solution species [60]. These diffusion controlled processes could cause limitations in the rate capability due to the increased solid/electrolyte interfacial resistance and/or diffusion constraints [61]. Except for the narrow potential regions around the redox peaks, the  $b$ -values of the major potentials are in the range of 0.8-1.0, showing more capacitive behaviour of the  $\text{Mn}_3\text{O}_4$  in APC-THF electrolyte. The kinetics analysis of the CV curves suggests a combined effect between the diffusion-controlled interfacial reactions involving the THF solvent and the surface-governed capacitive processes in the  $\text{Mn}_3\text{O}_4$  cathode.

To distinguish qualitatively between the capacitive and redox based contribution, the current response at a fixed potential can be expressed as the combination of surface capacitive effects ( $k_1v$ ) and diffusion-controlled processes ( $k_2v^{1/2}$ ):  $i(V) = k_1v + k_2v^{1/2}$  [21,22,62]. By determining both the  $k_1$  and  $k_2$  constants through the plots of  $v^{1/2}$  vs  $i v^{-1/2}$  in Fig. 9a, it is possible to quantify the fraction of contribution from each of these two processes [21]. As shown in Fig. 9b, the area under the CV curve represents the total stored charge that arises from both the diffusion-controlled and non-diffusion-controlled processes. A dominating capacitive contribution (the shade area) of ~77% is obtained. As the scan rate increases, the capacitive contribution becomes more pronounced in accordance with the more rectangular shape and more weakened redox peaks of the CV curves in Fig. 8a. As a consequence, similar to the supercapacitor, the charge/discharge limitation is mainly the transfer of ions and electrons to the surface plane of the electrode material rather than the ion diffusion in solid state. These findings should also be applicable to the synthesized  $Mn_3O_4$ -based nanocomposites, since their electrochemical behaviour was quite similar to that of the pure  $Mn_3O_4$  nanoparticles. Thus, the capacitive governed charge storage mechanism in the synthesized  $Mn_3O_4$ -based materials may account for their high rate capability and excellent long cycling stability (see Fig. 2 and Fig. 3). It is also a reasonable explanation for the close relationship between the electrochemical performance of the synthesized materials and the morphological features and surface properties.

#### 4. Conclusions

In conclusion, the capacitive-governed mechanism endows the synthesized  $Mn_3O_4$ -based materials with capacitor-characteristic performance (high rate capability and long cycling stability) in a Mg battery configuration. This makes it feasible to improve the electrochemical performance by controlling the morphology features and the surface properties of the electrode materials to maximize the active surface sites for charge storage. Thus, the *MRGO-4* nanocomposite with good dispersity of  $Mn_3O_4$  nanoparticles and the enhanced conductivity delivers a reversible capacity of ~220 mAh g<sup>-1</sup> at 15.4 mA g<sup>-1</sup> and ~80 mAh g<sup>-1</sup> at 1.54 A g<sup>-1</sup>, much higher than the pure  $Mn_3O_4$  nanoparticles (~100 mAh g<sup>-1</sup> at 15.4 mA g<sup>-1</sup> and ~20 mAh g<sup>-1</sup> at 1.54 A g<sup>-1</sup>). Another nanocomposite, *MGO*, which possesses the highest surface area and largest amount of functional groups among the synthesized composites, provides reversible capacities equivalent to the *MRGO-4* composite. These promising cell performances obtained from the capacitive-type cathodes broaden the selectivity of electrode materials which are limited by the sluggish solid-state Mg diffusion.

#### ■ ASSOCIATED CONTENT

##### Supporting Information

XRD patterns of the synthesized  $Mn_3O_4$  and nanocomposites. ATR-FTIR spectra of the synthesized samples. The selected area electron diffraction (SAED) patterns of the synthesized  $Mn_3O_4$  and nanocomposites. CV curves of the synthesized nanocomposites in APC-THF electrolyte at 0.2 mV s<sup>-1</sup>. Long cycle life of *MGO* at 308 mA g<sup>-1</sup>. The galvanostatic charge/discharge profiles of GO at 15.4 mA g<sup>-1</sup>. The charge storage performances of  $Mn_3O_4$ , *MGO* and *MRGO* electrodes in the symmetrical cell configuration, all the measurements were

carried out in 1M MgCl<sub>2</sub> aqueous electrolyte between 0 and 1 V. STEM/EDS/EELS characterizations of the magnesiated Mn<sub>3</sub>O<sub>4</sub> nanoparticles in APC-THF electrolyte. Specific and volumetric capacities of Mn<sub>3</sub>O<sub>4</sub> nanoparticles, *MGO* and *MRGO* nanocomposites at 15.4 mA g<sup>-1</sup>. Elemental analysis, specific surface area and electronic conductivity of the synthesized Mn<sub>3</sub>O<sub>4</sub> and nanocomposites.

## ■ AUTHOR INFORMATION

### Corresponding Author

\*E-mail: [fride.vullum-bruer@ntnu.no](mailto:fride.vullum-bruer@ntnu.no)

### Notes

The authors declare no competing financial interest.

## ■ ACKNOWLEDGMENTS

This work was sponsored by the Research Council of Norway through the project NanoMag (Grant no. 221785). Erachem Comilog is acknowledged for providing the commercial Mn<sub>3</sub>O<sub>4</sub> powders free of charge.

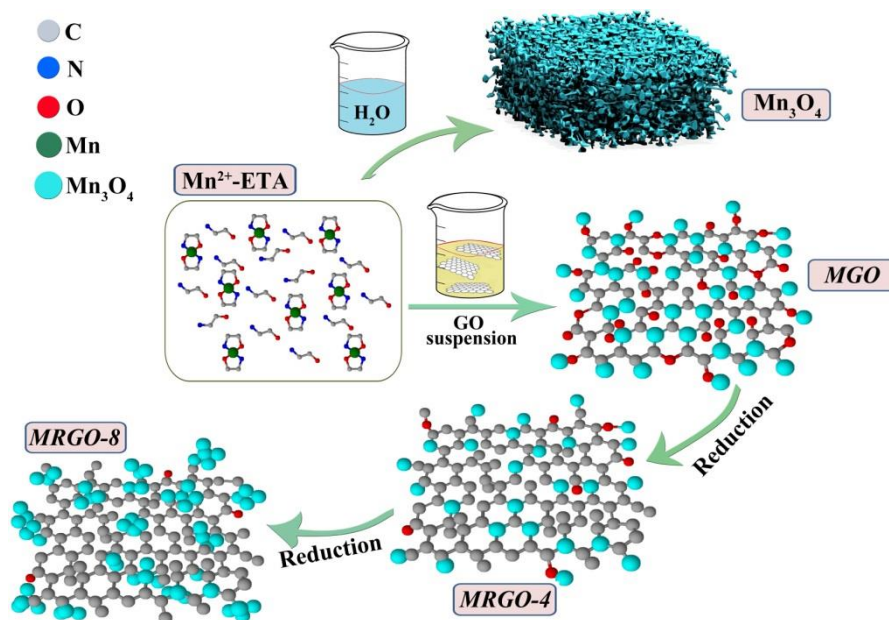
## ■ REFERENCES

- [1] J. Song, E. Sahadeo, M. Noked, S.B. Lee, *J. Phys. Chem. Lett.* 7 (2016) 1736-1749.
- [2] R. Zhang, X. Yu, K.W. Nam, C. Ling, T.S. Arthur, W. Song, A.M. Knapp, S.N. Ehrlich, X.Q. Yang, M. Matsui, *Electrochem. Commun.* 23 (2012) 110-113.
- [3] L. Wang, K. Asheim, P.E. Vullum, A.M. Svensson, F. Vullum-Bruer, *Chem. Mater.* 28 (2016) 6459-6470.
- [4] C. Ling, R.G. Zhang, T.S. Arthur, F. Mizuno, *Chem. Mater.* 27 (2015) 5799-5807.
- [5] J. Muldoon, C.B. Bucur, A.G. Oliver, J. Zajicek, G.D. Allred, W.C. Boggess, *Energy Environ. Sci.* 6 (2013) 482-487.
- [6] N. Wu, Z.Z. Yang, H.R. Yao, Y.X. Yin, L. Gu, Y.G. Guo, *Angew. Chem. Int. Ed.* 54 (2015) 5757-5761.
- [7] Y. Cheng, T. Liu, Y. Shao, M.H. Engelhard, J. Liu, G. Li, *J. Mater. Chem. A* 2 (2014) 2473-2477.
- [8] R.E. Doe, R. Han, J. Hwang, A.J. Gmitter, I. Shterenberg, H.D. Yoo, N. Pour, D. Aurbach, *Chem. Commun.* 50 (2014) 243-245.
- [9] E.N. Keyzer, H.F. Glass, Z. Liu, P.M. Bayley, S.E. Dutton, C.P. Grey, D.S. Wright, *J. Am. Chem. Soc.* 138 (2016) 8682-8685.
- [10] S.Y. Ha, Y.W. Lee, S.W. Woo, B. Koo, J.S. Kim, J. Cho, K.T. Lee, N.S. Choi, *Acs Appl. Mater. Interfaces* 6 (2014) 4063-4073.
- [11] R. Mohtadi, M. Matsui, T.S. Arthur, S.J. Hwang, *Angew. Chem. Int. Ed.* 51 (2012) 9780-9783.
- [12] D. Aurbach, Z. Lu, A. Schechter, Y. Gofer, H. Gizbar, R. Turgeman, Y. Cohen, M. Moshkovich, E. Levi, *Nature* 407 (2000) 724-727.
- [13] E. Lancry, E. Levi, Y. Gofer, M. Levi, G. Salitra, D. Aurbach, *Chem. Mater.* 16 (2004) 2832-2838.
- [14] P. Novak, W. Scheifele, O. Haas, *J. Power Sources* 54 (1995) 479-482.
- [15] M.E. Spahr, P. Novak, O. Haas, R. Nesper, *J. Power Sources* 54 (1995) 346-351.

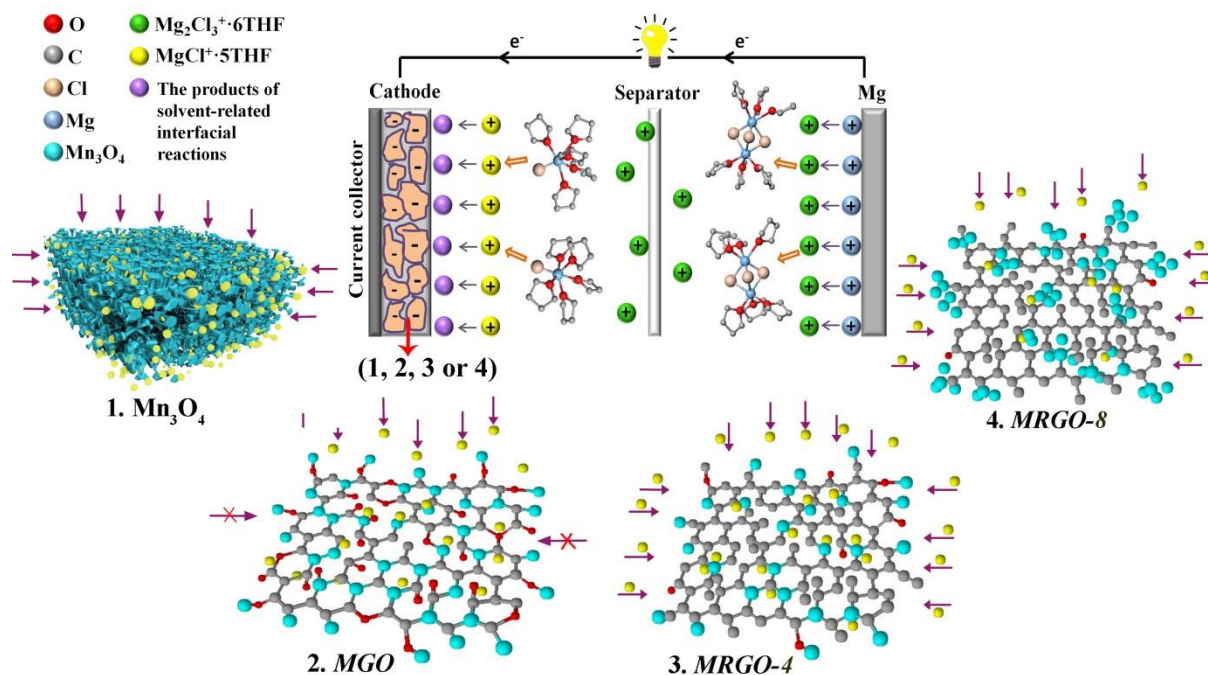
- [16] G. Gershinsky, H.D. Yoo, Y. Gofer, D. Aurbach, *Langmuir* 29 (2013) 10964-10972.
- [17] Y.L. Liang, R.J. Feng, S.Q. Yang, H. Ma, J. Liang, J. Chen, *Adv. Mater.* 23 (2011) 640-643.
- [18] Y.C. Liu, L.F. Jiao, Q. Wu, J. Du, Y.P. Zhao, Y.C. Si, Y.J. Wang, H.T. Yuan, *J. Mater. Chem. A* 1 (2013) 5822-5826.
- [19] L. Yu, X.G. Zhang, *J. Colloid Interf. Sci.* 278 (2004) 160-165.
- [20] X.Q. Sun, P. Bonnicksen, V. Duffort, M. Liu, Z.Q. Rong, K.A. Persson, G. Ceder, L.F. Nazar, *Energy Environ. Sci.* 9 (2016) 2273-2277.
- [21] J. Wang, J. Polleux, J. Lim, B. Dunn, *J. Phys. Chem. C* 111 (2007) 14925-14931.
- [22] D. Chao, C. Zhu, P. Yang, X. Xia, J. Liu, J. Wang, X. Fan, S.V. Savilov, J. Lin, H.J. Fan, Z.X. Shen, *Nat. Commun.* 7 (2016) 12122.
- [23] D. Chao, P. Liang, Z. Chen, L. Bai, H. Shen, X. Liu, X. Xia, Y. Zhao, S.V. Savilov, J. Lin, Z.X. Shen, *ACS Nano* 10 (2016) 10211-10219.
- [24] J. Xie, C. Li, Z. Cui, X. Guo, *Adv. Funct. Mater.* 25 (2015) 6519-6526.
- [25] Y. Zhang, J. Xie, Y. Han, C. Li, *Adv. Funct. Mater.* 25 (2015) 7300-7308.
- [26] P. Canepa, G.S. Gautam, R. Malik, S. Jayaraman, Z. Rong, K.R. Zavadil, K. Persson, G. Ceder, *Chem. Mater.* 27 (2015) 3317-3325.
- [27] C.J. Barile, R. Spatney, K.R. Zavadil, A.A. Gewirth, *J. Phys. Chem. C* 118 (2014) 10694-10699.
- [28] C.J. Barile, E.C. Barile, K.R. Zavadil, R.G. Nuzzo, A.A. Gewirth, *J. Phys. Chem. C* 118 (2014) 27623-27630.
- [29] L. Metsger, S. Bittner, *Tetrahedron* 56 (2000) 1905-1910.
- [30] T.J. Wang, Z.H. Ma, M.Y. Huang, Y.Y. Jiang, *Poly. Adv. Technol.* 7 (1996) 88-91.
- [31] M. Sommovigo, H. Alper, *J. Mol. Catal.* 88 (1994) 151-158.
- [32] A.K. Fazlurrahman, J.C. Tsai, K.M. Nicholas, *J. Chem. Soc. Chem. Comm.* (1992) 1334-1335.
- [33] N. Pour, Y. Gofer, D.T. Major, D. Aurbach, *J. Am. Chem. Soc.* 133 (2011) 6270-6278.
- [34] D.T. Nguyen, X.M. Tran, J. Kang, S.W. Song, *ChemElectroChem* 3 (2016) 1813-1819.
- [35] C.G. Liu, Z.N. Yu, D. Neff, A. Zhamu, B.Z. Jang, *Nano Lett.* 10 (2010) 4863-4868.
- [36] A. Sumboja, C.Y. Foo, X. Wang, P.S. Lee, *Adv. Mater.* 25 (2013) 2809-2815.
- [37] X.C. Dong, H. Xu, X.W. Wang, Y.X. Huang, M.B. Chan-Park, H. Zhang, L.H. Wang, W. Huang, P. Chen, *ACS Nano* 6 (2012) 3206-3213.
- [38] L.L. Zhang, R. Zhou, X.S. Zhao, *J. Mater. Chem.* 20 (2010) 5983-5992.
- [39] Y. Wang, Z.Q. Shi, Y. Huang, Y.F. Ma, C.Y. Wang, M.M. Chen, Y.S. Chen, *J. Phys. Chem. C* 113 (2009) 13103-13107.
- [40] W.S. Hummers, R.E. Offeman, *J. Am. Chem. Soc.* 80 (1958) 1339-1339.
- [41] L. Wang, Y.H. Li, Z.D. Han, L. Chen, B. Qian, X.F. Jiang, J. Pinto, G. Yang, *J. Mater. Chem. A* 1 (2013) 8385-8397.
- [42] H.D. Yoo, I. Shterenberg, Y. Gofer, G. Gershinsky, N. Pour, D. Aurbach, *Energy Environ. Sci.* 6 (2013) 2265-2279.
- [43] J.M. Montes, F.G. Cuevas, J. Cintas, P. Urban, *Appl. Phys. A* 105 (2011) 935-947.
- [44] H.L. Guo, X.F. Wang, Q.Y. Qian, F.B. Wang, X.H. Xia, *ACS Nano* 3 (2009) 2653-2659.
- [45] J. Zhang, H. Yang, G. Shen, P. Cheng, J. Zhang, S. Guo, *Chem. Comm.* 46 (2010) 1112-1114.
- [46] Z.Y. Lin, Y.G. Yao, Z. Li, Y. Liu, Z. Li, C.P. Wong, *J. Phys. Chem. C* 114 (2010) 14819-14825.
- [47] Y.X. Xu, H. Bai, G.W. Lu, C. Li, G.Q. Shi, *J. Am. Chem. Soc.* 130 (2008) 5856-5857.
- [48] S. Stankovich, R.D. Piner, X.Q. Chen, N.Q. Wu, S.T. Nguyen, R.S. Ruoff, *J. Mater. Chem.* 16 (2006) 155-158.
- [49] A. Benmayza, M. Ramanathan, T.S. Arthur, M. Matsui, F. Mizuno, J. Guo, P.A. Glans, J. Prakash, *J. Phys. Chem. C* 117 (2013) 26881-26888.
- [50] A. Pendashteh, M.F. Mousavi, M.S. Rahmanifar, *Electrochim. Acta* 88 (2013) 347-357.

- [51] H. Wang, Q. Hao, X. Yang, L. Lu, X. Wang, *Electrochem. Commun.* 11 (2009) 1158-1161.
- [52] S. Chen, J. Zhu, X. Wu, Q. Han, X. Wang, *ACS Nano* 4 (2010) 2822-2830.
- [53] B. Yuan, C. Xu, D. Deng, Y. Xing, L. Liu, H. Pang, D. Zhang, *Electrochim. Acta* 88 (2013) 708-712.
- [54] C.T. Hsieh, H. Teng, *Carbon* 40 (2002) 667-674.
- [55] B. Xu, S. Yue, Z. Sui, X. Zhang, S. Hou, G. Cao, Y. Yang, *Energy Environ. Sci.* 4 (2011), 2826-2830.
- [56] H.Y. Tan, J. Verbeeck, A. Abakumov, G. Van Tendeloo, *Ultramicroscopy* 116 (2012) 24-33.
- [57] V. Augustyn, P. Simon, B. Dunn, *Energy Environ. Sci.* 7 (2014) 1597-1614.
- [58] H. Lindstrom, S. Sodergren, A. Solbrand, H. Rensmo, J. Hjelm, A. Hagfeldt, S.E. Lindquist, *J. Phys. Chem. B* 101 (1997) 7717-7722.
- [59] M. Sathiya, A.S. Prakash, K. Ramesha, J.M. Tarascon, A.K. Shukla, *J. Am. Chem. Soc.* 133 (2011) 16291-16299.
- [60] B.E. Conway, V. Birss, J. Wojtowicz, *J. Power Sources* 66 (1997) 1-14.
- [61] M. Park, X.C. Zhang, M.D. Chung, G.B. Less, A.M. Sastry, *J. Power Sources* 195 (2010) 7904-7929.
- [62] T.C. Liu, W.G. Pell, B.E. Conway, S.L. Roberson, *J. Electrochem. Soc.* 145 (1998) 1882-1888.

## Schemes and Figures



**Scheme 1.** Preparation routes of  $\text{Mn}_3\text{O}_4$  nanoparticles,  $\text{MGO}$  and  $\text{MRGO}$  nanocomposites.



**Scheme 2.** Illustration of the proposed magnesiaion processes for the  $\text{Mn}_3\text{O}_4$  nanoparticles,  $\text{MGO}$  and  $\text{MRGO}$  nanocomposite cathodes in a Mg battery.

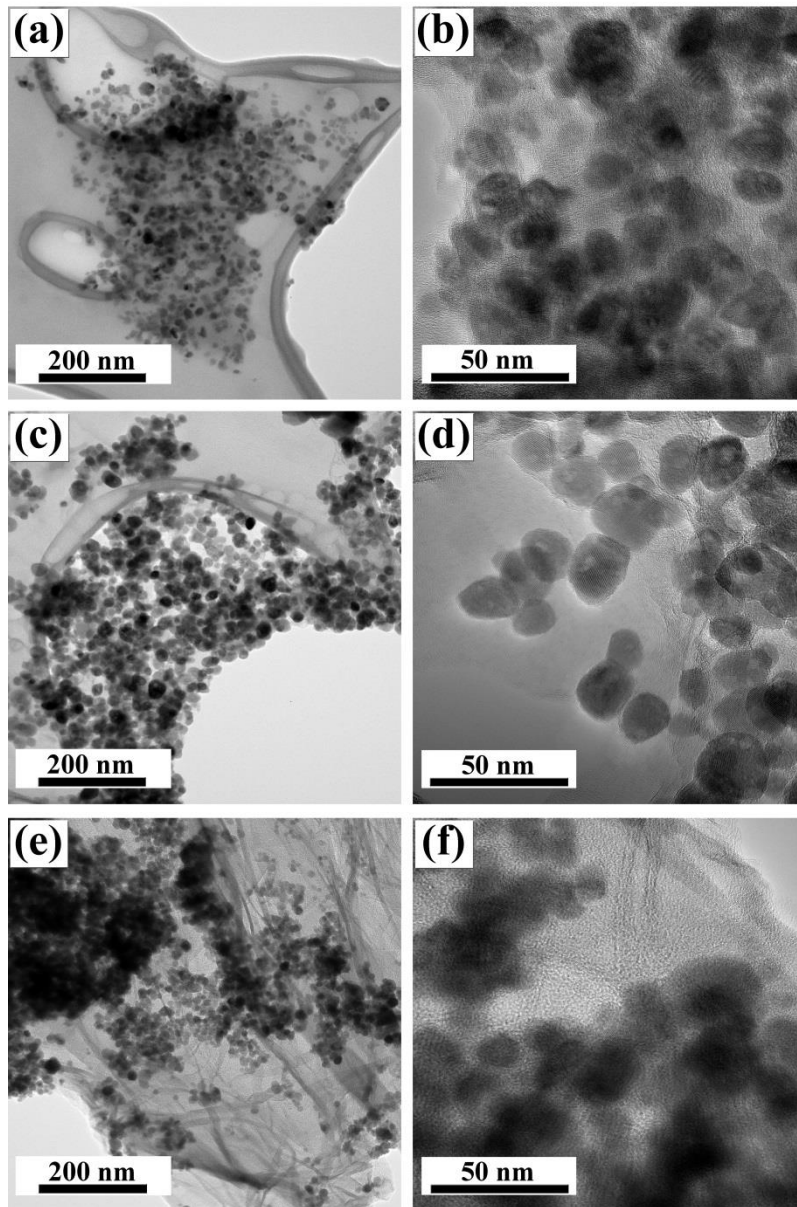


**Fig. 1.** Typical bright field (BF) TEM images of (a and b) *MGO*, (c and d) *MRGO-4*, and (e and f) *MRGO-8* nanocomposites.

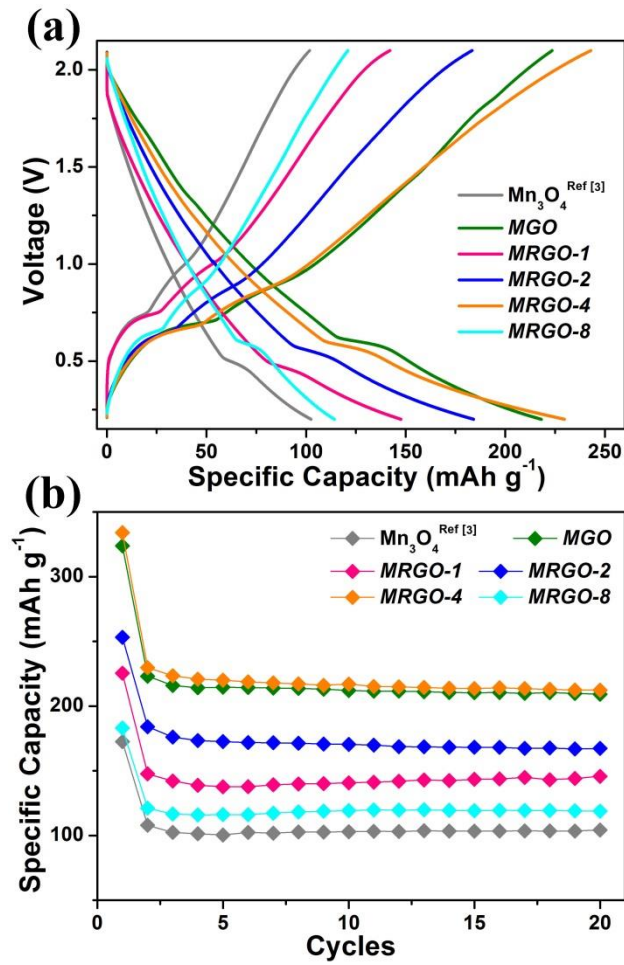


**Fig. 2.** The cell performances of  $\text{Mn}_3\text{O}_4$ , MGO and MRGO cathodes of a Mg battery: (a) galvanostatic charge/discharge profiles, and (b) cycling stability at  $15.4 \text{ mA g}^{-1}$ . The electrochemical data of  $\text{Mn}_3\text{O}_4$  is referred from our previous work (Ref [3]) and shown for comparison.

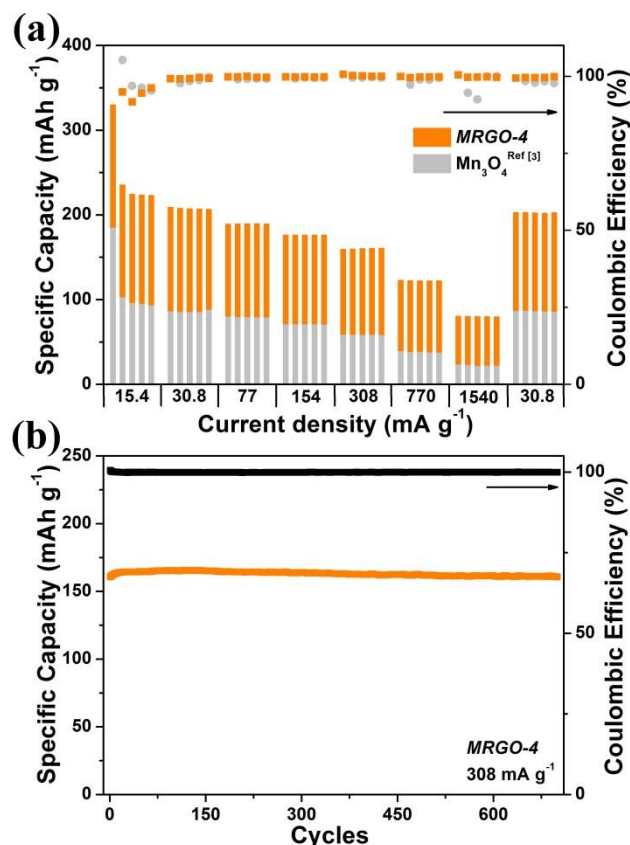


**Fig. 3.** (a) Rate cyclic performance of *MRGO-4*. The rate performance of  $\text{Mn}_3\text{O}_4$  is referred from our previous work (Ref [3]) and shown for comparison. (b) Long cycle life of *MRGO-4* at  $308 \text{ mA g}^{-1}$ .

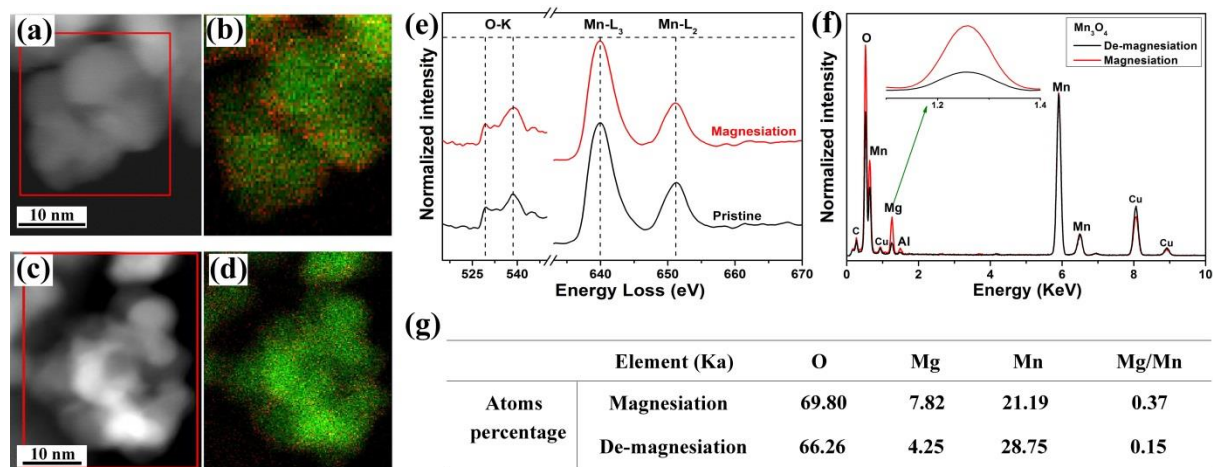


**Fig. 4.** High angle annular dark field (HAADF) images with EDS mappings (Mg-red and Mn-green, corresponding to the marked area in the HAADF image) of (a,b) magnesiated, (c,d) demagnesiated  $\text{Mn}_3\text{O}_4$  nanoparticles (which is synthesized by the ultrasonic-assisted method in this work) in APC-THF electrolyte. The corresponding EDS mappings of Mn, O and Mg are shown in Fig.S8. (e) Mn-L<sub>2,3</sub> and O-K edges spectra of the pristine and magnesiates  $\text{Mn}_3\text{O}_4$ . (f) EDS spectra and (g) atoms percentages of Mg, Mn, O in magnesiates and demagnesiates  $\text{Mn}_3\text{O}_4$  nanoparticles.

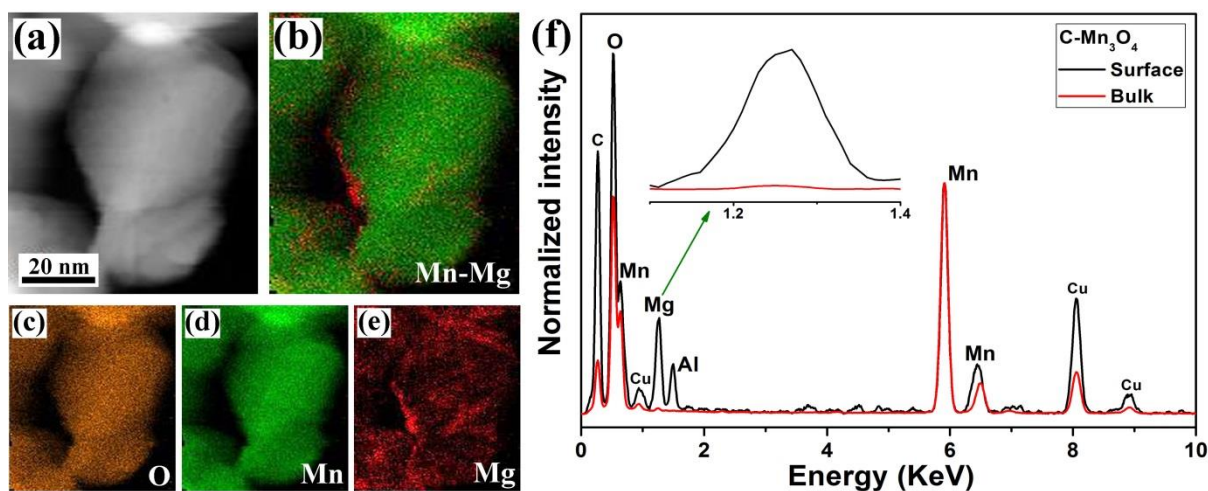


**Fig. 5.** (a) HAADF images of the magnesiated C-Mn<sub>3</sub>O<sub>4</sub> nanoparticles (the commercial Mn<sub>3</sub>O<sub>4</sub>) in APC-THF electrolyte, and the corresponding (b) overlaid Mn-Mg map, (c) O map, (d) Mn map and (e) Mg map. (f) The comparison of EDS spectra between the surface and the bulk of the magnesiated C-Mn<sub>3</sub>O<sub>4</sub> cathode, inset shows the enlarged part of the Mg peaks.

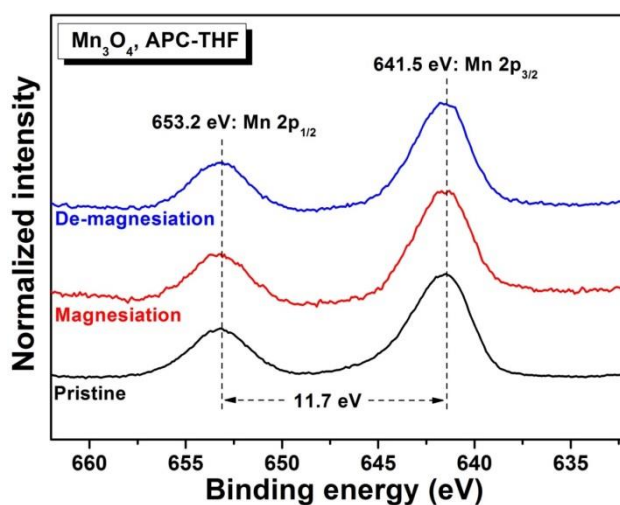


**Fig. 6.** XPS Mn 2p spectra of Mn<sub>3</sub>O<sub>4</sub> cathodes at different cell states in APC-THF electrolyte.

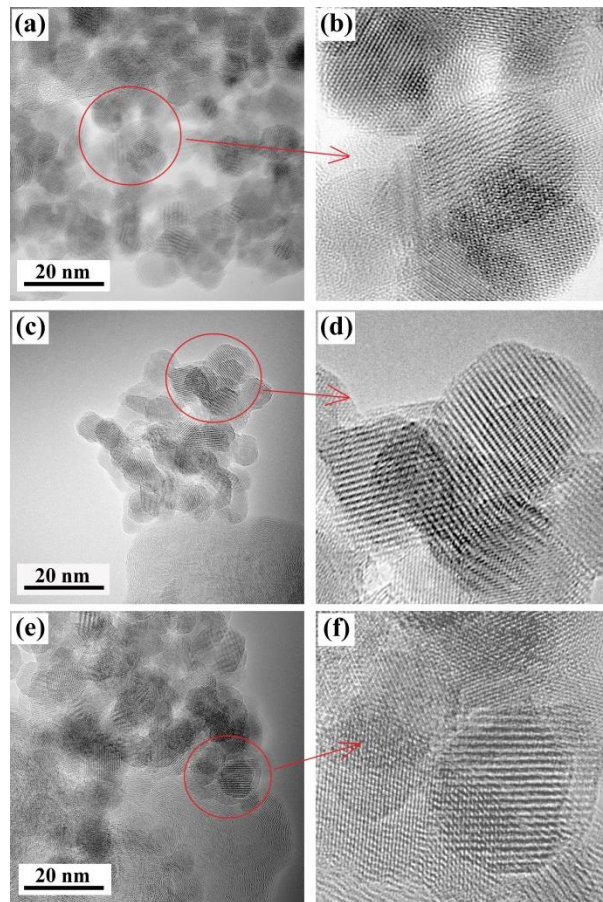


**Fig. 7.** *Ex-situ* TEM images of  $\text{Mn}_3\text{O}_4$  cathodes at (a,b) pristine, (c,d) magnesiated and (e,f) demagnesiated states in APC-THF electrolyte.

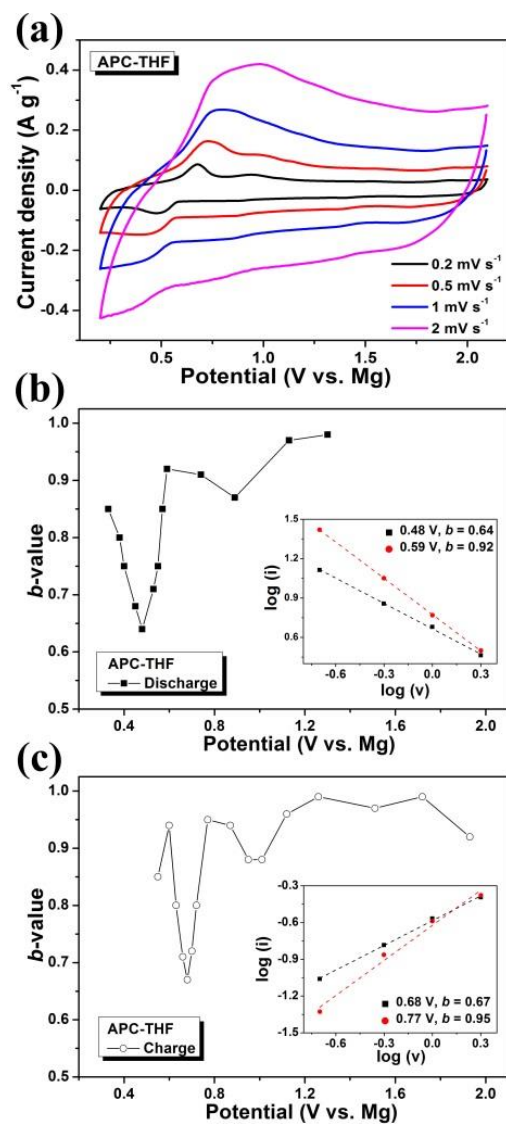


**Fig. 8.** (a) CV curves of  $\text{Mn}_3\text{O}_4$  cathode at different scan rates in APC-THF electrolyte. The CV curve of  $\text{Mn}_3\text{O}_4$  is referred from our previous work (Ref [3]) and shown for comparison. The dependence of  $b$ -values as a function of potential for (b) anodic sweeps and (c) cathodic sweeps, respectively. Insets show the power law dependence of current as a function of sweep rate.

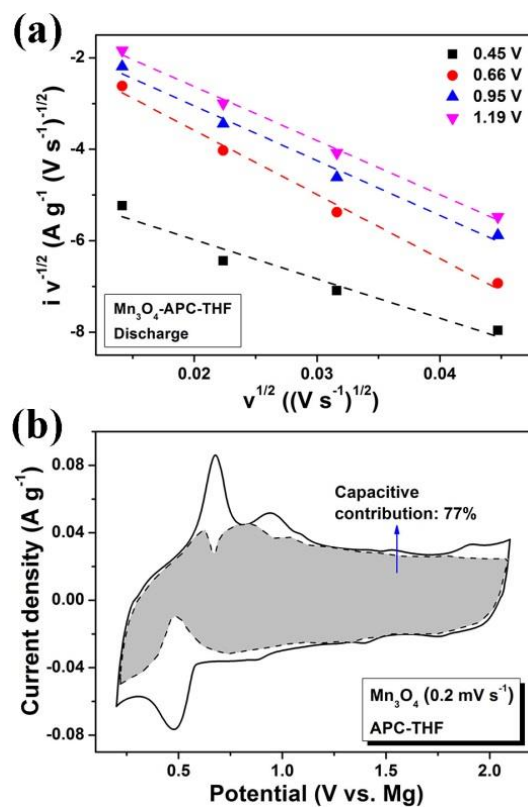


**Fig. 9.** (a) Plots of  $v^{1/2}$  vs  $i v^{-1/2}$ ,  $v$  varies from 0.2 to 2  $\text{mV s}^{-1}$ . (b) The capacitive contribution (the shaded region) to the total voltammetric response current at  $0.2 \text{ mV s}^{-1}$ .

## Electronic Supplementary Information (ESI)

### High Capacity Mg Batteries Based on Surface-Controlled Electrochemical Reactions

Lu Wang,<sup>a</sup> Per Erik Vullum,<sup>b,c</sup> Karina Asheim,<sup>a</sup> Xuehang Wang,<sup>d</sup> Ann Mari Svensson,<sup>a</sup> and Fride Vullum-Bruer<sup>\*a</sup>

<sup>a</sup>Department of Materials Science and Engineering, Norwegian University of Science and Technology, NO-7491 Trondheim, Norway

<sup>b</sup>SINTEF Materials and Chemistry, 7491 Trondheim, Norway

<sup>c</sup>Department of Physics, Norwegian University of Science and Technology, 7491 Trondheim, Norway

<sup>d</sup>Department of Chemical Engineering, Norwegian University of Science and Technology, 7491 Trondheim, Norway.

\*Corresponding Authors. E-mail: [fride.vullum-bruer@ntnu.no](mailto:fride.vullum-bruer@ntnu.no)

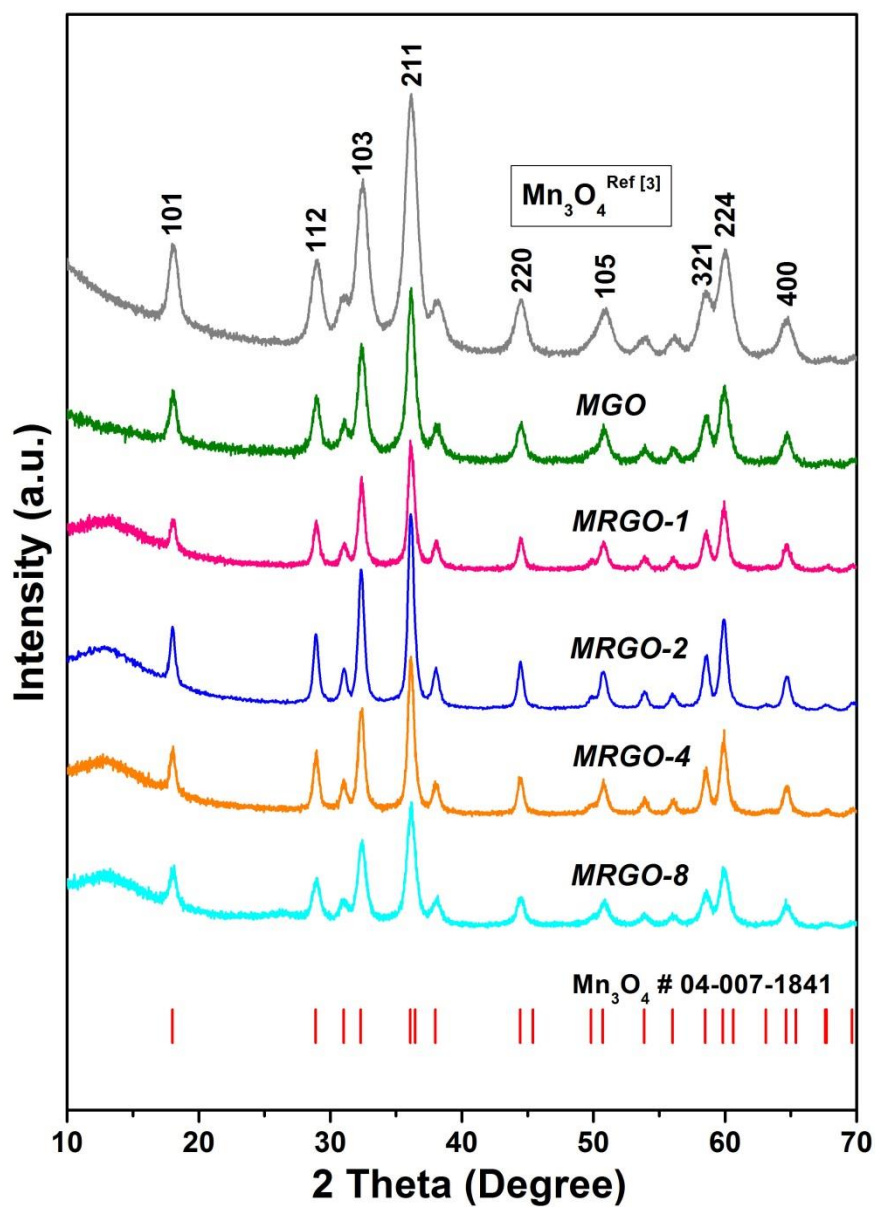


**Fig. S1.** XRD patterns of the synthesized nanocomposites. The XRD pattern of Mn<sub>3</sub>O<sub>4</sub> is referred from our previous work (Ref [3]) and shown for comparison.

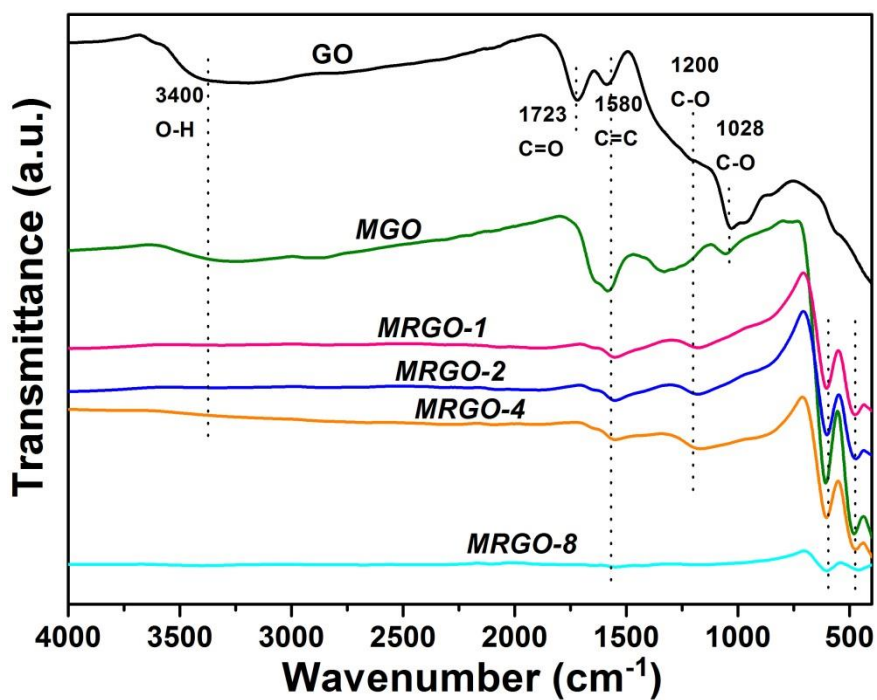


**Fig. S2.** ATR-FTIR spectra of the synthesized samples.

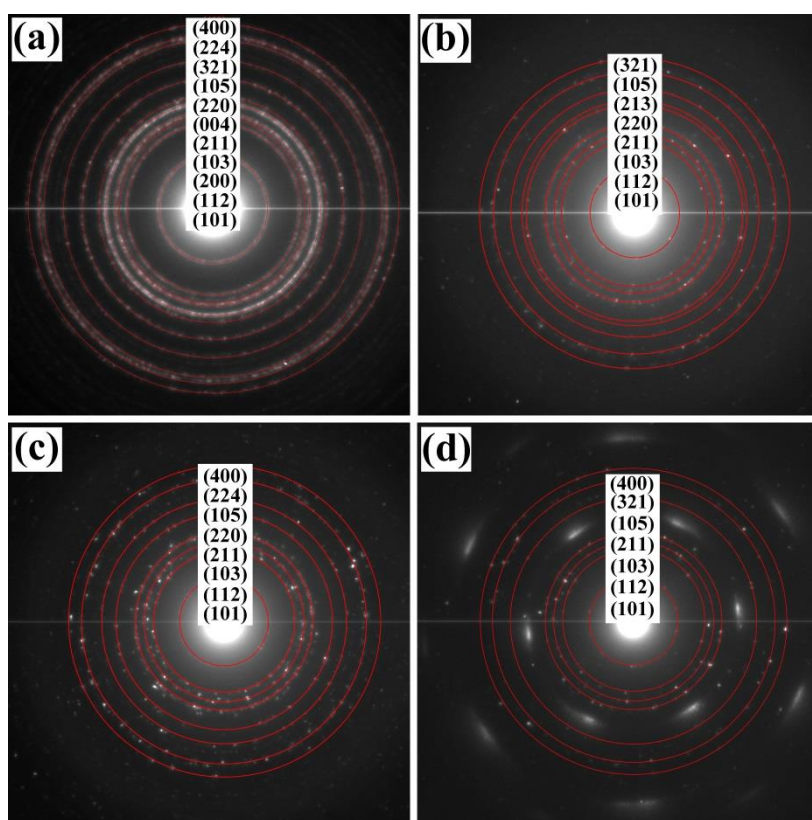


**Fig. S3.** The selected area electron diffraction (SAED) patterns of (a)  $\text{Mn}_3\text{O}_4$  nanoparticles, (b) MGO, (c) MRGO-4, and (d) MRGO-8 nanocomposites.

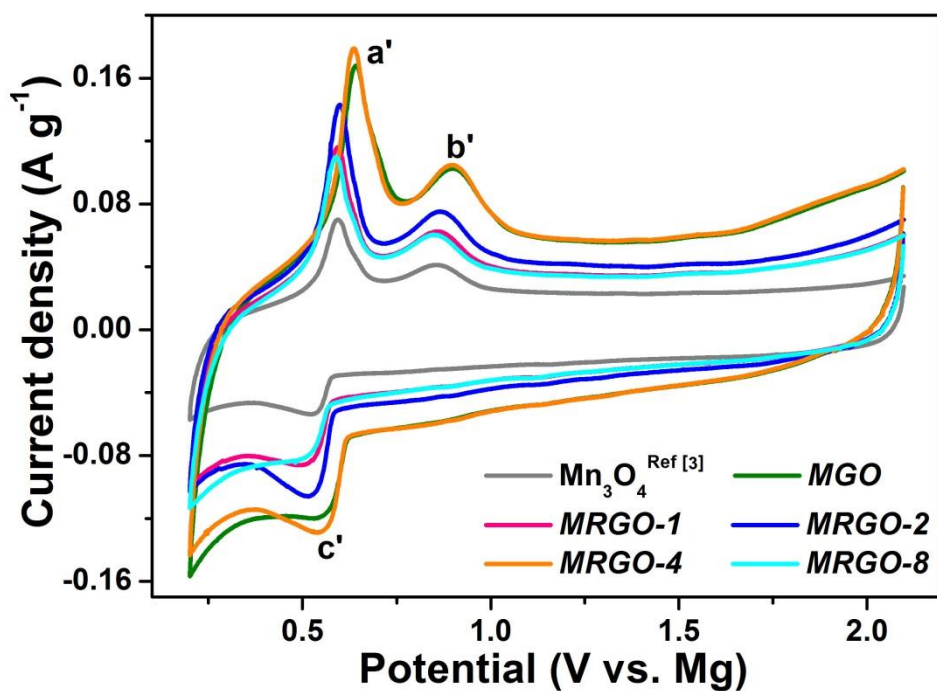


**Fig. S4.** CV curves of the synthesized nanocomposites in APC-THF electrolyte at  $0.2 \text{ mV s}^{-1}$ . CV curve of  $\text{Mn}_3\text{O}_4$  is referred from our previous work (Ref [3]) and shown for comparison. The slight anodic peak (a' and b') shift is probably caused by the different morphology features and surface properties of the synthesized materials.

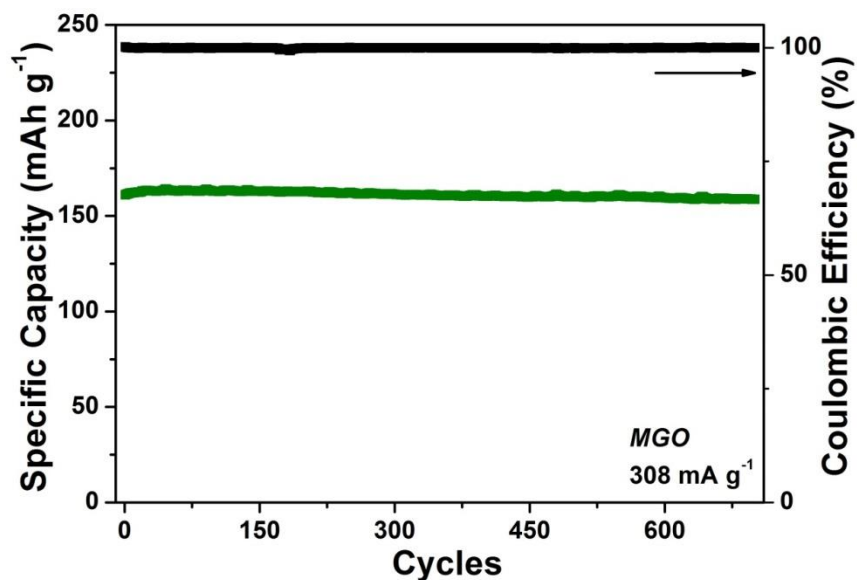


**Fig. S5.** Long cycle life of *MGO* at  $308 \text{ mA g}^{-1}$ .

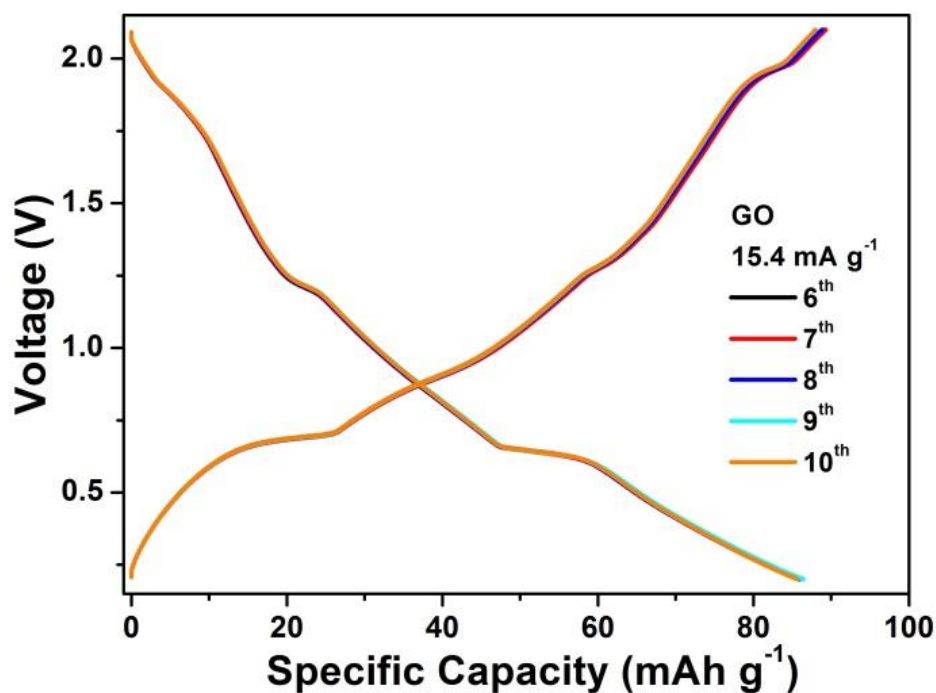


**Fig. S6.** The galvanostatic charge/discharge profiles of GO at  $15.4 \text{ mA g}^{-1}$ .

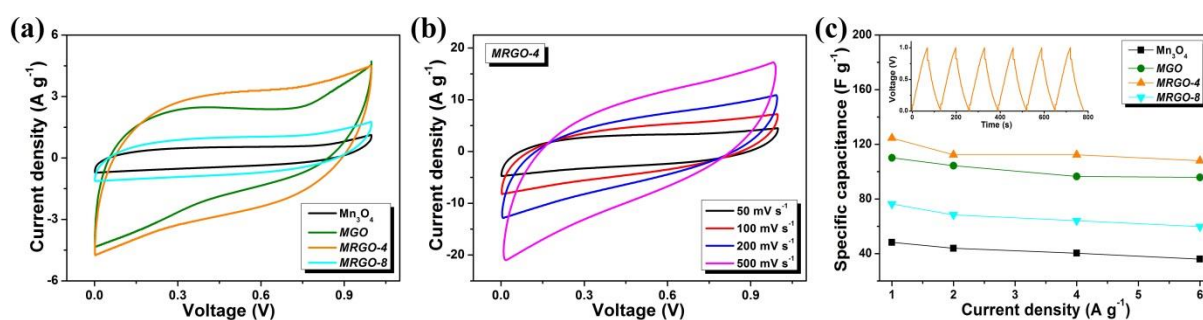


**Fig. S7.** The charge storage performances of  $\text{Mn}_3\text{O}_4$ , *MGO* and *MRGO* electrodes in the symmetrical cell configuration, all the measurements were carried out in  $1\text{M MgCl}_2$  aqueous electrolyte between 0 and 1 V: (a) Comparison of CV curves at  $50 \text{ mV s}^{-1}$ . (b) CV curves of *MRGO-4* at varying scan rates. (c) Plot of specific capacitance as a function of charge rates. Inset: Galvanostatic charge/discharge curve of *MRGO-4* at  $4 \text{ A g}^{-1}$ .

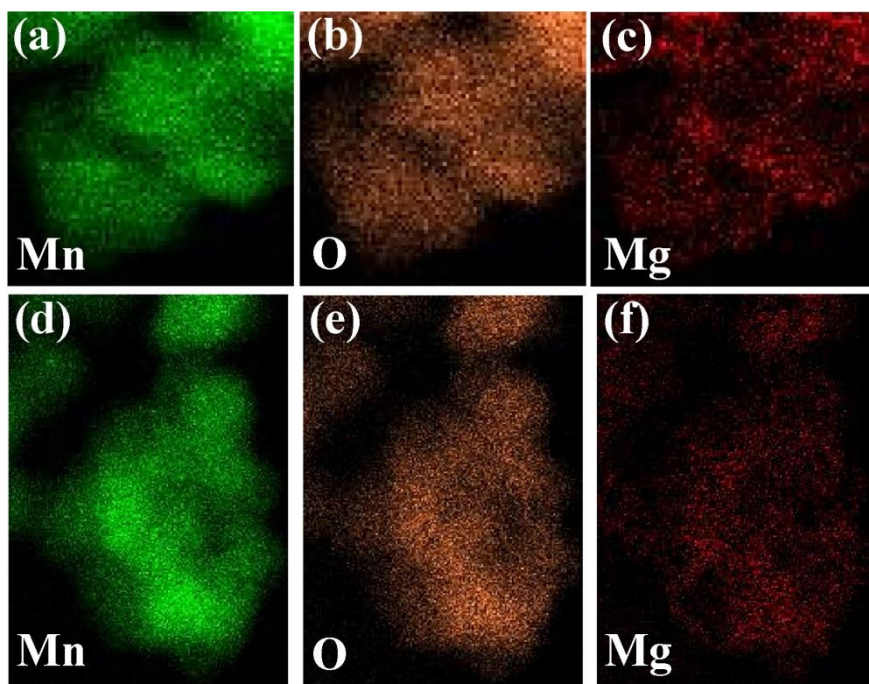


**Fig. S8.** (a) Mn map, (b) O map and (c) Mg maps of  $\text{Mn}_3\text{O}_4$  nanoparticles that shown in Fig. 4a. (d) Mn map, (e) O map and (f) Mg maps of  $\text{Mn}_3\text{O}_4$  nanoparticles that shown in Fig.4c.

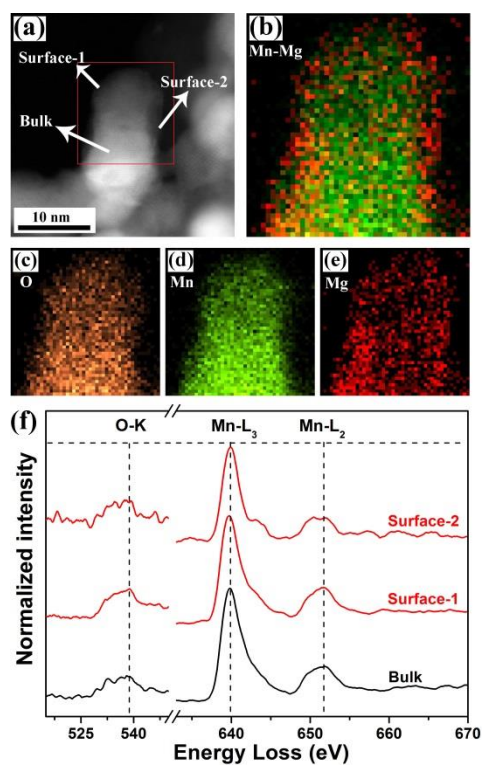


**Fig. S9.** (a) HAADF STEM image of the magnesiated  $\text{Mn}_3\text{O}_4$  cathode in APC electrolyte, and the corresponding EDS mappings of (b) Mn-Mg, (c) O, (d) Mn and (e) Mg. (f) Comparison of the Mn  $L_{2,3}$  and the O-K edges between the surface part and the bulk part of the magnesiated  $\text{Mn}_3\text{O}_4$  cathodes.

**Table S1.** Specific and volumetric capacities of  $\text{Mn}_3\text{O}_4$  nanoparticles, *MGO* and *MRGO* nanocomposites at  $15.4 \text{ mA g}^{-1}$

	$\text{Mn}_3\text{O}_4$	<i>MGO</i>	<i>MRGO-1</i>	<i>MRGO-2</i>	<i>MRGO-4</i>	<i>MRGO-8</i>
<sup>a</sup> Specific capacities	~100	~220	~150	~180	~220	~115
<sup>b</sup> Specific capacities	~80	~176	~120	~144	~176	~92
<sup>c</sup> volumetric capacity	~21	~47	~32	~38	~47	~25

<sup>a</sup> Specific capacities ( $\text{mAh g}^{-1}$ ) are related to the mass of the active materials

<sup>b</sup> Specific capacities ( $\text{mAh g}^{-1}$ ) are related to the mass of the electrode materials

<sup>c</sup> Volumetric capacities ( $\text{mAh mL}^{-1}$ ) were obtained based on the approximate thickness of the electrode film of around  $15 \mu\text{m}$ . The low volumetric capacities ( $\sim 20\text{-}50 \text{ mAh mL}^{-1}$ ) are caused by the fact that the charge storage in the studied cell system is surface-dependent.

**Table S2.** Elemental analysis, specific surface area and electronic conductivity of  $\text{Mn}_3\text{O}_4$  nanoparticles, *MGO* and *MRGO* nanocomposites

Sample	C wt%	H wt%	N wt%	C/H	C/N	BET ( $\text{m}^2 \text{g}^{-1}$ )	Conductivity ( $\text{S m}^{-1}$ )
$\text{Mn}_3\text{O}_4$	-	-	-	-	-	102	$4.18 \cdot 10^{-5}$
<i>MGO</i>	8.64	0.97	1.25	8.91	6.91	159	$6.45 \cdot 10^{-6}$
<i>MRGO-1</i>	8.17	0.75	0.82	10.9	9.96	123	$9.13 \cdot 10^{-2}$
<i>MRGO-2</i>	8.76	0.76	0.8	11.5	10.9	127	$2.55 \cdot 10^{-1}$
<i>MRGO-4</i>	7.76	0.63	0.7	12.3	11.1	121	1.41
<i>MRGO-8</i>	15.3	0.56	0.24	27.4	63.8	118	2.44